

Ca II 8542 Å brightenings induced by a solar microflare[★]

C. Kuckein¹, A. Diercke^{1,2}, S. J. González Manrique^{3,1,2}, M. Verma¹,
J. Löhner-Böttcher⁴, H. Socas-Navarro⁵, H. Balthasar¹, M. Sobotka⁶, and C. Denker¹

- ¹ Leibniz-Institut für Astrophysik Potsdam (AIP), An der Sternwarte 16, 14482 Potsdam, Germany
e-mail: ckuckein@aip.de
² Universität Potsdam, Institut für Physik und Astronomie, Karl-Liebknecht-Str. 24/25, 14476 Potsdam, Germany
³ Astronomical Institute of the Slovak Academy of Sciences, 05960 Tatranská Lomnica, Slovak Republic
⁴ Kiepenheuer-Institut für Sonnenphysik, Schöneckstr. 6, 79104 Freiburg, Germany
⁵ Instituto de Astrofísica de Canarias, Avda vía Láctea S/N, 38205 La Laguna, Tenerife, Spain
⁶ Astronomical Institute, Academy of Sciences of the Czech Republic, Fričova 298, 25165 Ondřejov, Czech Republic

Received 6 June 2017 / Accepted 14 September 2017

ABSTRACT

Aims. We study small-scale brightenings in Ca II 8542 Å line-core images to determine their nature and effect on localized heating and mass transfer in active regions.

Methods. High-resolution two-dimensional spectroscopic observations of a solar active region in the near-infrared Ca II 8542 Å line were acquired with the GREGOR Fabry-Pérot Interferometer attached to the 1.5-m GREGOR telescope. Inversions of the spectra were carried out using the NICOLE code to infer temperatures and line-of-sight (LOS) velocities. Response functions of the Ca II line were computed for temperature and LOS velocity variations. Filtergrams of the Atmospheric Imaging Assembly (AIA) and magnetograms of the Helioseismic and Magnetic Imager (HMI) were coaligned to match the ground-based observations and to follow the Ca II brightenings along all available layers of the atmosphere.

Results. We identified three brightenings of sizes up to $2'' \times 2''$ that appeared in the Ca II 8542 Å line-core images. Their lifetimes were at least 1.5 min. We found evidence that the brightenings belonged to the footpoints of a microflare (MF). The properties of the observed brightenings disqualified the scenarios of Ellerman bombs or Interface Region Imaging Spectrograph (IRIS) bombs. However, this MF shared some common properties with flaring active-region fibrils or flaring arch filaments (FAFs): (1) FAFs and MFs are both apparent in chromospheric and coronal layers according to the AIA channels; and (2) both show flaring arches with lifetimes of about 3.0–3.5 min and lengths of $\sim 20''$ next to the brightenings. The inversions revealed heating by 600 K at the footpoint location in the ambient chromosphere during the impulsive phase. Connecting the footpoints, a dark filamentary structure appeared in the Ca II line-core images. Before the start of the MF, the spectra of this structure already indicated average blueshifts, meaning upward motions of the plasma along the LOS. During the impulsive phase, these velocities increased up to -2.2 km s^{-1} . The structure did not disappear during the observations. Downflows dominated at the footpoints. However, in the upper photosphere, slight upflows occurred during the impulsive phase. Hence, bidirectional flows are present in the footpoints of the MF.

Conclusions. We detected Ca II brightenings that coincided with the footpoint location of an MF. The MF event led to a rise of plasma in the upper photosphere, both before and during the impulsive phase. Excess mass, previously raised to at most chromospheric layers, slowly drained downward along arches toward the footpoints of the MF.

Key words. Sun: photosphere – Sun: chromosphere – Sun: corona – Sun: activity – techniques: imaging spectroscopy

1. Introduction

Small-scale and intense short-lived brightenings are often seen in the solar atmosphere. These impulsive events are frequently hypothesized to form as a result of magnetic reconnection, which if true would mean that they also produce local heating. In the past, such events were mainly studied with ground-based facilities. Today, space-borne telescopes have become powerful tools especially in combination with new high-resolution ground-based data. This ensures unprecedented multiwavelength analyses of impulsive events across many layers of the solar atmosphere.

There are several types of similar-looking brightenings, which increases the difficulty of understanding these phenomena and their relation (e.g., Rutten et al. 2013). Fundamental

differences in their lifetime, size, location, expansion along the atmosphere, and other characteristic observational signatures distinguish these events, however.

The by far most frequently studied small-scale brightenings are Ellerman bombs (EBs), which have been introduced by Ellerman (1917) as “solar hydrogen bombs”. From an observational point of view, they are intensity enhancements of the H α line wings, while the line core remains unaffected. The same applies to the Ca II 8542 Å line (Fang et al. 2006b), even though exceptions are possible (Rezaei & Beck 2015). No signature is observed higher up in the corona (Schmieder et al. 2004). Together with evidence that EBs are best identified in 1600 and 1700 Å filtergrams (Berlicki et al. 2010; Pariat et al. 2007; Vissers et al. 2013), these facts suggest that they are located in the photosphere (Rutten et al. 2013), although discrepancies about their formation height still exist (e.g., Berlicki & Heinzel 2014). Their lifetimes are usually shorter than 30 min, predominantly between

[★] The movie associated to Fig. 2 is available at <http://www.aanda.org>

1.5 and 7 min with a peak between 3 and 4 min (Pariat et al. 2007; Vissers et al. 2013), although longer-lived EBs have been detected (Bello González et al. 2013). EBs are typically located in active regions, surrounded by magnetic field concentrations or at polarity inversion lines (e.g., Matsumoto et al. 2008; Nelson et al. 2013; Reid et al. 2016), and have a small elongated shape with typical sizes of $1''.8 \times 1''.1$ (Georgoulis et al. 2002). EBs lead to temperature enhancements of up to 600–1300 K, derived from observational Ca II 8542 Å data (Fang et al. 2006b). Recent ground-based high-resolution observations probably indicate that even smaller EBs exist ($0''.3$ – $0''.8$) with temperature increments of up to 3000 K (Li et al. 2015). Owing to these previous results, it is widely considered that EBs result from magnetic reconnection (Vissers et al. 2013, and references therein).

An extensive amount of literature has been published on microflares (MFs). They are small highly energetic brightenings. MFs are often observed as hard X-ray bursts, are short lived (2.2–15 min; Hannah et al. 2008), and can occur every 5 min in active regions during solar maximum (Lin et al. 1984). Moreover, precursor brightenings have been detected in light curves of 1600 Å (Brosius & Holman 2009). The apparent chromospheric counterpart of an MF in H α (Canfield & Metcalf 1987; Liu et al. 2004) shows fine structure and sizes of a few arcseconds (Berkebile-Stoiser et al. 2009). Fang et al. (2006a) reported on emission cores in H α and Ca II 8542 Å intensity spectra during MFs. These authors inferred temperature increments of about 1000–2200 K in the lower chromosphere during the MFs. This increment is in accordance with the observed line-core emission of Ca II 8542 Å. High bidirectional velocities between $\pm(40$ – $50)$ km s $^{-1}$ were derived using the Ca II 8542 Å line (Hong et al. 2016). Microflares are frequently found near magnetic polarity inversion lines (Liu et al. 2004).

A new class of brightening was recently discovered with the space-borne Interface Region Imaging Spectrograph (IRIS; De Pontieu et al. 2014). The so-called IRIS bombs (IBs) consist of small roundish pockets of photospheric hot gas. Peter et al. (2014) reported on transient features with lifetimes of about 5 min that occur in active regions where magnetic fields cancel. These brightenings resemble EBs, with the difference that they manifest in much higher photospheric temperatures (up to 100 000 K). In an independent analysis, Judge (2015) proposed that these bombs are rather located higher, in the low- to mid-chromosphere. Nevertheless, it has been shown that some EBs are co-spatial to IBs (Tian et al. 2016). As a consequence, if IBs are directly related to EBs, existing models might underestimate the temperature increments of the latter (<3000 K; Li et al. 2015). The formation height of EBs might play an important role when determining their temperature. In coronal filtergrams from the Atmospheric Imaging Assembly (AIA; Lemen et al. 2012) no indication of IBs are found.

Few data are published on flaring arch filaments. Vissers et al. (2015) defined them as small brightenings with an elongated morphology that have shorter lifetimes than EBs. However, Rutten (2016) suggested a more accurate name for these events: “flaring active-region fibrils” (FAFs), in order to avoid confusion with larger filaments. FAFs are well identified in 1600 Å filtergrams, while their appearance, in contrast to EBs, is not always clear in 1700 Å images. Vissers et al. (2015) studied two FAFs in detail and concluded that (1) FAFs occur in active regions; (2) they probably indicate magnetic reconnection but higher in the atmosphere than EBs; (3) they show a fibril-like morphology; and (4) they produce bright arches in the hotter chromosphere and corona. Pariat et al. (2009) reported

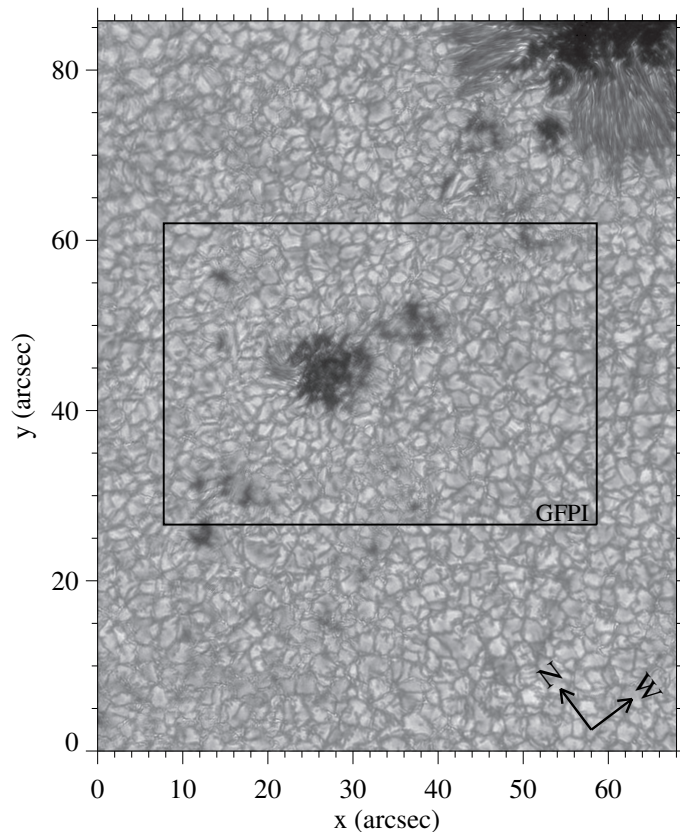


Fig. 1. Speckle-restored blue continuum (4505 Å) image of active region NOAA 12149 at 08:38 UT on 2014 August 26 observed with the PCO.4000 CCD camera installed in the blue imaging channel of the GFPI at GREGOR. The rectangle outlines the FOV of the GFPI. Arrows in the bottom right-hand corner indicate solar north and west.

“transient loops” in 1600 Å images that probably are FAFs. In the past, FAFs were already studied, but no common name was suggested so far. As pointed out by Rutten (2016), FAFs are very similar to EBs with the difference that they also affect the higher atmospheric layers.

In this work, we report on high-resolution ground-based observations using Ca II 8542 Å imaging spectra in an active region. The observations include three small brightening areas of the near-infrared Ca II line core that are carefully discussed and placed into context using space observations. Temperature and Doppler velocity statistics inferred from spectral-line inversions are presented.

2. Observations

The observations were carried out on 2014 August 26 with the 1.5-m GREGOR solar telescope (Schmidt et al. 2012) located on Tenerife, Spain. We observed a group of pores in active region NOAA 12149 at coordinates $(x, y) = (-240'', 40'')$ and cosine of heliocentric angle $\mu \sim 0.97$, close to the solar disk center (Fig. 1). The pores show opposite polarity to the leading sunspot. The primary instrument was the GREGOR Fabry-Pérot Interferometer (GFPI). The GFPI is equipped with two synchronized cameras. One records continuum images in the broad-band channel, the other observes spectral narrow-band images filtered by two etalons in the collimated beam. We refer to Puschmann et al. (2012) and references therein for a complete

overview of the GFPI. The setup allows for image restoration using multi-object multi-frame blind deconvolution (MOMFBD; Löfdahl 2002; van Noort et al. 2005).

The GFPI was operated in the imaging spectroscopic mode with a prefilter centered at the Ca II 8542 Å line. Since the quantum efficiency of the detector substantially decreases when approaching the upper limit of 8600 Å, exposure times of 80 ms were necessary. Four accumulations were performed for each of the selected 36 wavelength positions. A nonuniform step size was chosen to scan the Ca II line. The wings were sampled wider with a step size of 200 mÅ, while the inner wings and line core were sampled narrower with 80 mÅ, spanning a total spectral window of 4.6 Å. The individual spectral positions with respect to the Ca II 8542 Å line-core center were: -2.22, -2.02, -1.82, -1.62, -1.41, -1.21, -1.01, -0.81, -0.73, -0.65, -0.56, -0.48, -0.40, -0.32, -0.24, -0.16, -0.08, 0.00, 0.08, 0.16, 0.24, 0.32, 0.40, 0.48, 0.56, 0.65, 0.73, 0.81, 1.01, 1.21, 1.41, 1.62, 1.82, 2.02, 2.22, and 2.42 Å.

We acquired 20 scan sequences, starting at 08:23:57 UT and ending at 08:39:25 UT, with a cadence of 47 s. The field of view (FOV) of the GFPI was 52'' × 36'', with an image scale of ~0'081 pixel⁻¹ in the 2 × 2-pixel binning mode.

A context image is provided by the PCO.4000 CCD camera installed in the blue imaging channel of the GFPI (Fig. 1). The camera was equipped with a blue continuum filter (4505 Å) and acquired 80 images in one burst. The FOV was 68'' × 86'', with an image scale of about 0'035 pixel⁻¹.

In support of our ground-based observations, we analyzed data from the Solar Dynamics Observatory (SDO; Pesnell et al. 2012). We focused on filtergrams recorded by AIA in the wavelength bands 131, 94, 335, 211, 193, 171, 304, 1600, and 1700 Å. These wavelengths give us the opportunity to track any event across different temperatures and heights in the solar atmosphere, from the photosphere to the corona. The cadence for 1600 and 1700 Å data was 24 s, while all other channels were acquired with a cadence of 12 s. Furthermore, magnetograms from the Helioseismic and Magnetic Imager (HMI; Scherrer et al. 2012) with a cadence of 45 s were used to complement the filtergrams with information of the line-of-sight (LOS) magnetic field.

3. Data reduction and analysis

The ground-based data were reduced using the reduction pipeline “sTools” (Kuckein et al. 2017). It included dark and flat-field corrections for both instruments. In addition, for GFPI, blueshift, prefilter transmission corrections, and a continuum adjustment of the spectral profile by matching it with an atlas profile from the Fourier transform spectra (FTS; Neckel & Labs 1984) spectrometer were performed. The image restoration of GFPI’s broad-band channel using MOMFBD was successful. Unfortunately, the algorithm delivered unsatisfactory Ca II 8542 Å narrow-band images. We ascribe this to the relatively low signal-to-noise ratio of the data. Nevertheless, a comparison between the spectral profiles arising from the restored and non-restored images in our data set showed negligible changes. Therefore our study was carried out with the non-restored Ca II spectroscopic images. The speckle-interferometry code KISIP (Wöger & von der Lühe 2008) was used to restore the blue continuum images. Image rotation induced by the altitude-azimuth mount of the telescope (Volkmer et al. 2012) was removed.

3.1. GFPI wavelength calibration

We calculated the median intensity profile inside an area of 135 × 240 pixels (~11'' × 19''). This area was located in the right-hand bottom part of the FOV, in the absence of magnetic structures as seen in the HMI magnetogram. A polynomial fit to the line core of this profile yielded the central position. We considered the central position as the wavelength at rest of the Ca II line, which we established at 8542.09 Å (Kramida et al. 2015). The theoretical dispersion of the GFPI was 4.04 mÅ position⁻¹ at 8542 Å. We computed the wavelength array by multiplying the 36 scan positions along the line by the dispersion. We are limited to this calibration since a more accurate wavelength calibration needed nearby telluric lines or synthetic laser lines.

3.2. Solar dynamics observatory

We started with processed Level 1.0 data from AIA and HMI for the time period between 08:00–09:00 UT. Level 1.0 implies a basic data reduction, that is, flat-field correction and conversion into FITS format (Lemen et al. 2012). Further processing steps are carried out with the “Solar Software” routines (SSW; Freeland & Handy 1998; Bentely & Freeland 1998), like the adjustment of the image scale of HMI to AIA (0'5 → 0'6 pixel⁻¹) (DeRosa & Slater 2013). The alignment of the data was carried out with the SSW routines to derotate the images with respect to the central image of the time series at 08:30 UT.

All SDO data were then coaligned to the GFPI FOV (Fig. 2). This is achieved by vertical mirroring, magnification, rotation (~37°), and shifting of the corresponding FOV of SDO.

3.3. Ca II 8542 Å inversions

To deeper investigate the Ca II spectra, we used the inversion code NICOLE (Socas-Navarro et al. 2015) to infer the physical parameters of the atmosphere where the line was formed. This includes temperatures and LOS velocities at several optical depths, that is, at different heights. The code carries out non-local thermodynamical equilibrium (NLTE) inversions of Zeeman-induced Stokes profiles. Its robustness and good performance using the Ca II 8542 Å line was demonstrated in recent works (e.g., de la Cruz Rodríguez et al. 2012, 2013; Leenaarts et al. 2014; Quintero Noda et al. 2016). Since we only recorded intensity profiles (Stokes *I*), we set the other Stokes parameters (*Q*, *U*, and *V*) to zero as well as their weights.

NICOLE needs an initial-guess atmosphere to compute the arising intensity profiles and compare them with the observed ones. Several initial atmospheres were tested, and the best fits to the observed intensity profiles were achieved with the Harvard-Smithsonian reference atmosphere (HSRA; Gingerich et al. 1971). The HSRA covers a wide range of heights, which are defined in terms of the logarithm of the LOS continuum optical depth τ at a wavelength of 5000 Å, and it spans the interval between $-8.0 \leq \log \tau \leq 1.4$. Hence, it extends from the photosphere to the transition region. The initial macro-turbulence was set to 2 km s⁻¹, to ensure smoother synthesized profiles, and was left as degree of freedom. We weighted the 36 spectral positions to concentrate only on the 23 points in the inner part of the Ca II line, in the range $-0.8 \leq \Delta\lambda \leq 1.2$ Å from the line center. The outer wings of the spectral line were omitted, only taking the outermost point on each side into account. This was motivated by the relatively slow cadence of one spectral scan (47 s). In the presence of dynamic events, the spectral

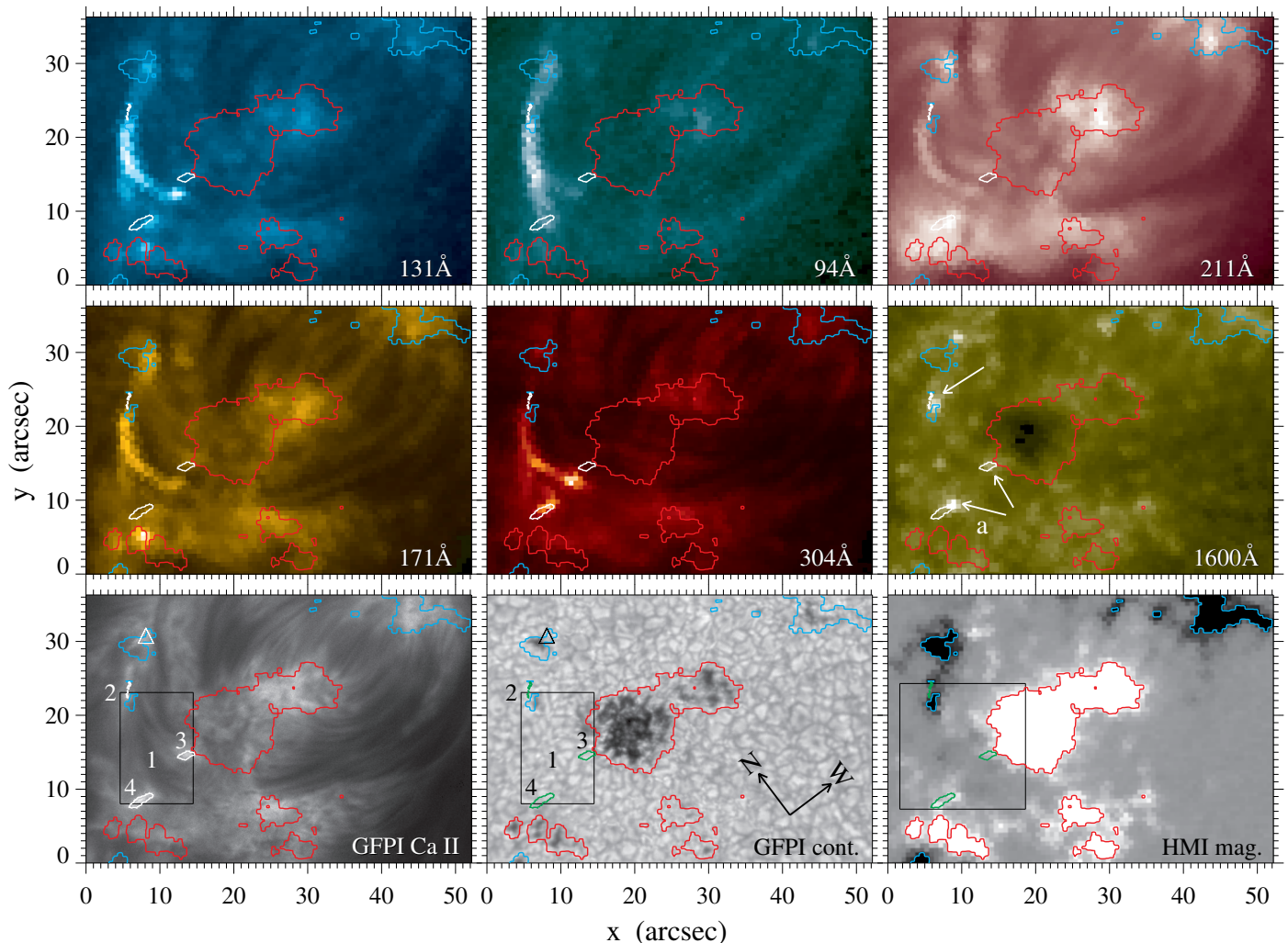


Fig. 2. Active region NOAA 12149 observed with SDO and GFPI. SDO images are shown for the time period 08:37:23–08:37:50 UT. The GFPI filtergrams correspond to 08:38:13 UT. Blue and red contours mark the negative and positive polarities, respectively, obtained from the HMI magnetogram saturated to ± 350 G in the *lower right panel*. The white contours (green in the case of the *two bottom rightmost images*), which are enumerated with numbers 2–4, correspond to the brightenings in the GFPI Ca II line-core image between 08:37–08:39 UT. Number 1 marks an area of dark filamentary structure as seen in the Ca II line-core image. The box in the HMI panel shows the FOV of the magnetograms in Fig. 4. The rectangle in the GFPI panels outlines the FOV of the inversions shown in Figs. 5 and 6. The triangle in the upper left corner of the GFPI panels highlights a persistent enhancement of the Ca II line core. The arrows in the AIA 1600 Å panel indicate three areas with sudden brightenings. The temporal evolution of this figure is shown between 08:35:08 and 08:39:08 in an [online movie](#).

profile might undergo substantial changes during the scan. By concentrating only on the line core and inner wings, we achieved better fits with NICOLE and still ensured a reliable temperature stratification.

Following the recommendation of [Leenaarts et al. \(2014\)](#), who reported on the effects of various isotopes of Ca with slightly different energies, we included the effects of isotopic splitting in NICOLE. We used up to 11 nodes for the temperature and 8 nodes for the LOS velocity. This version of NICOLE is unique compared to other similar inversion codes in that it uses a regularization scheme that ensures that smoother solutions are preferred. Thus, we only needed to ensure that the number of nodes was sufficiently large to provide the freedom necessary to fit the profiles. In practice, however, the number of degrees of freedom is smaller than the number of nodes because the regularization effectively reduces the freedom. Therefore, if the number of nodes is large enough, reducing it will not change the solution

significantly until the nodes are too few and there is not enough freedom to fit the observations. The magnetic field was not taken into account. In addition, three inversion sequences with five, three, and again three inversion attempts each, respectively, were chosen as part of the inversion strategy. The goodness of the fits were evaluated using the χ^2 value, which is defined as the sum of the squared difference between the observed and the synthesized intensity profiles. The lower the χ^2 value, the better the fit. The resulting atmosphere from the first inversion was used as input for the second inversion sequence, and so on. As expected, mostly, but not always, the third inversion sequence provided the lowest χ^2 and hence best result. Moreover, a visual inspection of the fits to the observed spectra was carried out to ensure the code's performance. We kept the best result of the three cycles with the lowest χ^2 value. A threshold of $\chi^2 \leq 0.008$ was chosen after visually examining very many random fits to ensure good-quality fits. Inversions with larger χ^2 were dropped (less than

3.5% of the pixels). In the physical maps in Figs. 5 and 6, the excluded pixels were substituted by the median of the surrounding 3×3 pixel mosaic.

An inversion of the whole FOV in all available maps was not possible. The inversion strategy for the NLTE inversions with NICOLE was, from a computational point of view, very time consuming. However, it provided the most reliable results. Therefore, we concentrated on a smaller FOV of 123×187 pixels ($\sim 10'' \times 15''$), which included the most relevant features in the Ca II line-core and SDO images. In this smaller FOV, we monitored the changes in temperature and LOS velocity. The FOV is outlined with a black rectangle at the GFPI panels in the bottom of Fig. 2.

3.3.1. Response functions

The Ca II 8542 Å spectral line extends across several layers of the solar atmosphere. The line core lies in the chromosphere, whereas the outer wings reach the photosphere. By computing response functions (RFs) to perturbations of the temperature and LOS velocity of a given atmospheric model, we infer at which atmospheric heights (in $\log \tau$ units) the Ca II line changes most noticeably in that model. The larger the RF, the higher the sensitivity of the spectral line to perturbations of a given physical quantity at a specific height. This allows focusing our analysis of the temperatures and LOS velocities on the relevant height ranges.

We followed the approach of Quintero Noda et al. (2016) to compute numerical RFs by perturbing the atmosphere at each $\log \tau$ value by a small amount. This was executed separately for each of the relevant physical parameters, like temperature and velocity, by adding 1 K and 10 m s^{-1} , respectively, to the initial model. The results differ from model to model. In our case, we used the HSRA model as the reference atmosphere. As described before, we only selected the inner wings and line core of the Ca II line ($-0.8 \leq \Delta\lambda \leq 1.2 \text{ Å}$ from the line core). For the LOS velocity, high values of the RF were detected between $-4.2 \geq \log \tau \geq -5.8$, corresponding to the chromosphere. In addition, an enhanced RF was retrieved in the upper photosphere within the height range $-2.7 \geq \log \tau \geq -3.9$. In the RFs for the temperature, high values were encountered in the chromosphere between $-4.4 \geq \log \tau \geq -5.2$. Moreover, the spectral line is sensitive to temperature changes in the photosphere between $-1.0 \geq \log \tau \geq -3.7$ (with a gradually decreasing RF with height). In line with Quintero Noda et al. (2016), we found a lower response of the Ca II line at around $\log \tau = -4$ in both RFs.

3.4. Line-of-sight velocities

In addition to the height-dependent LOS velocities inferred with NICOLE, we also performed Lorentzian fits with four coefficients to the Ca II 8542 Å line core between $-0.8 \leq \Delta\lambda \leq 0.8 \text{ Å}$ from the line center following the method described by González Manrique et al. (2016). The four coefficients represent the peak value, centroid, half-width at half-maximum, and a constant related to the continuum. This technique is not as reliable as carrying out spectral line inversions (Socas-Navarro et al. 2006) since the shape of the Ca II 8542 Å line undergoes significant changes in active regions. However, a comparison between this fast technique and the time-consuming inversions provides feedback on the reliability of this method.

4. Results

We concentrated our investigations on small brightening events detected at 08:37 UT as an enhancement of the Ca II 8542 Å line-core intensity in the GFPI data. The brightenings are marked with numbers 2–4 in all figures. We closely follow their origin and evolution in all AIA wavelength bands as well as with HMI LOS magnetograms. The Ca II spectra provide valuable information about the temperatures and LOS velocities inferred with the NICOLE inversion code.

4.1. Ca II 8542 Å line-core enhancements

The observations targeted a $\sim 10''$ wide pore with a rudimentary penumbra protruding from the left-hand side of the central part of the pore. A continuum image is shown in the bottom panel of Fig. 2. The contours outline the positive (red) and negative (blue) polarities taken from the HMI magnetogram clipped at $\pm 350 \text{ G}$ (shown in the bottom right panel of Fig. 2).

During the about 16-min observations, the penumbra was slowly evolving, but no expansion was evident. However, in the third to last scan (scan 18), we observed a sudden spectral enhancement of the Ca II line-core intensity at two spatial locations with sizes of about $1'' \times 1''$ and $2'' \times 2''$, areas 3 and 4 in the GFPI Ca II panel in Fig. 2. The scan started at 08:37:03 UT, and the line core of Ca II (which was sampled a few seconds after the start of the scan) appeared in emission. Approximately 1.5 min later, in the last scan (scan 20), a third location (area 2) clearly showed Ca II line-core emission. The three brightening areas are overplotted as white or green contours in Fig. 2. In addition, area 1 stands for a darker filamentary structure, with deep Ca II absorption, seen in the bottom GFPI panel, which we discuss below. The area marked with a triangle in the GFPI panels (upper left corner, at coordinates $(x, y) \sim (8'', 31'')$) also presents an enhancement of the Ca II line core. However, in contrast to the brightenings in areas 2–4, the enhancement is persistent during the 20 scans.

A closer inspection of the spectral profiles is plotted in Fig. 3. Each row shows one representative profile from areas 1–4. For reference, the quiet-Sun spectrum (dotted line) is also shown. It results from computing the median of 50 000 profiles in a quiet-Sun area on the right-hand side of the FOV. The first column corresponds to the first scan with the GFPI (08:24 UT). It is the farthest away in time ($\sim 13 \text{ min}$) from the beginning of the brightenings and hence represents a quiet atmosphere. The next three columns show the start of the brightenings. In the following, we call this nascent emission of the line core the “impulsive phase”. While areas 3 and 4 reach the impulsive phase already in scan 18, area 2 reaches a clear line-core emission later, as is best seen in scan 20. The Ca II impulsive phase lasts at least 1.5 min. Unfortunately, no additional observations were taken after scan 20.

In area 1, that is, in the dark filamentary structure, the intensity profiles appear blueshifted in all scans (top panels of Fig. 3). The spectrum becomes significantly asymmetric in scan 18, which corresponds to the beginning of the impulsive phase. Importantly, the Ca II line core does not turn into a clear emission at any time in this area during the temporal period we observed. For a further understanding of this impulsive event, we discuss these findings in the context of space data from SDO in the next sections.

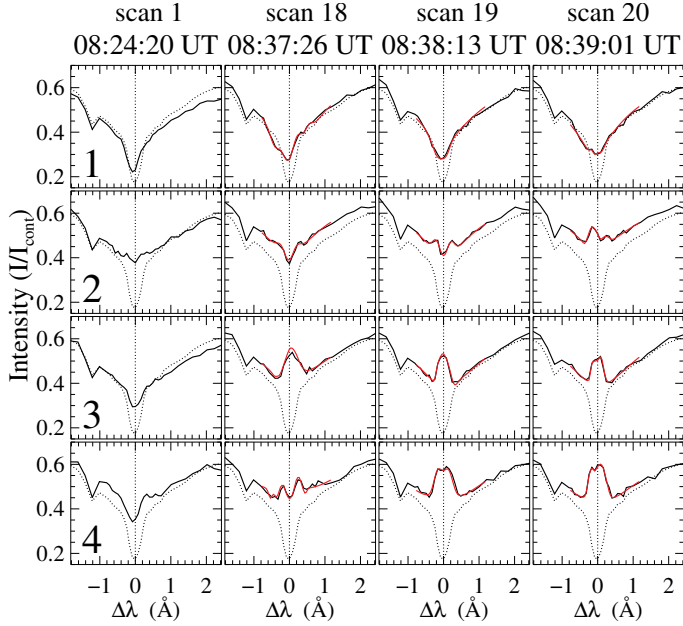


Fig. 3. Evolution (left to right) of the Ca II 8542 Å intensity profile (solid black line) displayed for the most conspicuous scans (1 and 18 to 20) in four selected areas (1–4, top to bottom). The four areas are also marked in all other figures. Overplotted in solid red is the best fit from the NICOLE inversions in the spectral range $-0.8 \leq \Delta\lambda \leq 1.2$ Å. The same pixel was chosen for each scan. The time corresponds to the midpoint of each scan. For reference, the dotted profile shows the average quiet-Sun profile.

4.2. AIA response to the impulsive event

We visually inspected all AIA wavelength bands and focused on the time between 08:35–08:42 UT (some channels are available as an online movie between 08:35:08 and 08:39:08 UT). In addition, we computed light curves of a smaller region of interest (not shown). A sudden and strong single brightening patch of about $2'' \times 2''$ was clearly detected in all AIA images at 08:37 UT (the exact position is marked with an arrow with letter “a” in the AIA 1600 Å panel of Fig. 2). The position partially overlaps with brightening area 4 from the GFPI. Its lifetime was very short (<1 min). Similar to the Ca II line-core enhancements of the GFPI, the AIA 1600 Å images also show three areas (almost cospatial with the Ca II areas) that suddenly became brighter simultaneously (three arrows in Fig. 2), but in contrast to Ca II (>1.5 min), quickly disappeared. Only a small increase in intensity was found in AIA 1700 Å images when thoroughly inspecting the light curve. In contrast, all other wavelength bands exhibited steep increases of their intensity. In the time range of 12–24 s after the strong single brightening patch, a double arch-shaped brightening became visible in all AIA channels except at 1600 and 1700 Å (Fig. 2). These two wavelengths belong substantially to lower heights in the solar atmosphere (Table 1 in Lemen et al. 2012). Except for a slight shift, the very bright arch is almost cospatial to the dark filamentary structure of area 1 in the Ca II line-core images. According to the AIA channels that sample the hottest layers, the flaring arches were visible for a duration of about 3.0–3.5 min. Their length was around $20''$. Spontaneous smaller post-flaring events were subsequently detected. Interestingly, AIA 304 Å images already showed occasional bright areas at least 30 min before the impulsive event of 08:37 UT. The other coronal wavelength bands also showed

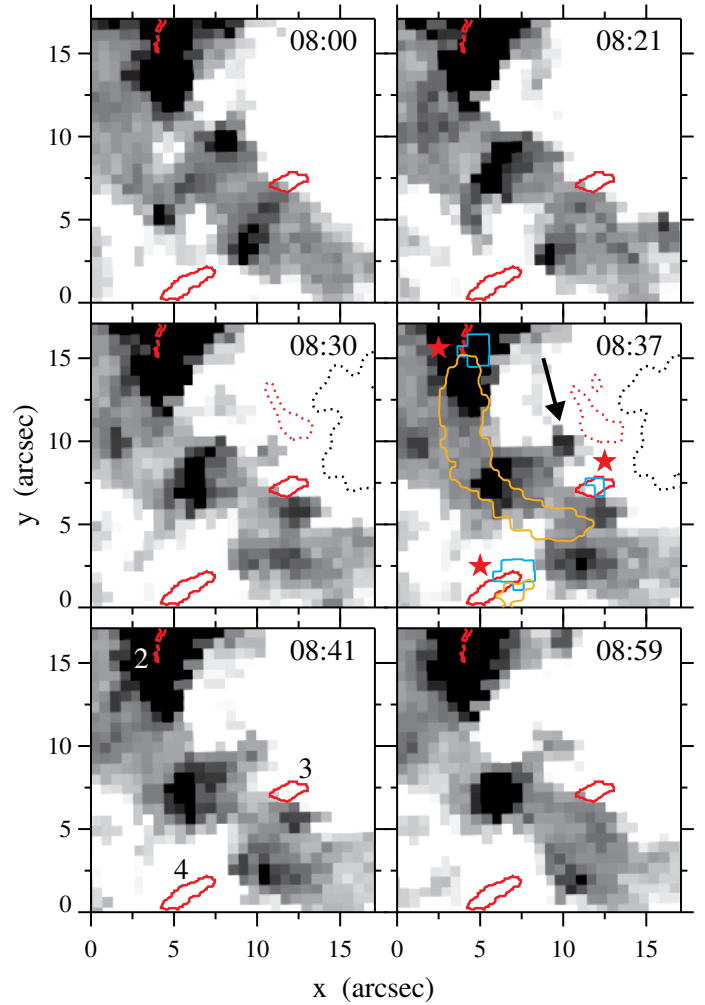


Fig. 4. HMI LOS magnetograms clipped between ± 40 G at selected times from 08:00 until 09:00 UT. The FOV corresponds to the black rectangle in the magnetogram panel of Fig. 2. The contours show the following: blue represents AIA 1600 Å brightenings, orange marks the flaring arch in AIA 131 Å, red shows the GFPI Ca II 8542 Å line-core brightenings, and dotted black and red represents the pore and forming penumbra, respectively. All contours refer to their time except the Ca II brightenings, which are static in all panels. The arrow at 08:37 UT points toward a newly appearing negative polarity. The three red stars next to the red contours indicate the beginning and location of the impulsive phase.

occasional but fainter brightenings outside of the described region of interest.

4.3. HMI magnetograms

Selected HMI LOS magnetograms between 08:00–09:00 UT are depicted in Fig. 4. A smaller region of interest was chosen (rectangle in the magnetogram panel of Fig. 2). The magnetograms were clipped at ± 40 G to better visualize very faint photospheric magnetic-field concentrations. A concentration of negative (black) polarity surrounded by positive (white) polarities was present on all sides. The red solid contours are permanently present in all panels and encompass Ca II profiles with line-core enhancements between 08:37–08:39 UT (same as the white or green contours in Fig. 2). The other contours vary according to their time stamp. Dynamic changes in central negative polarity were seen between 08:00 and 08:21 UT in the top panels

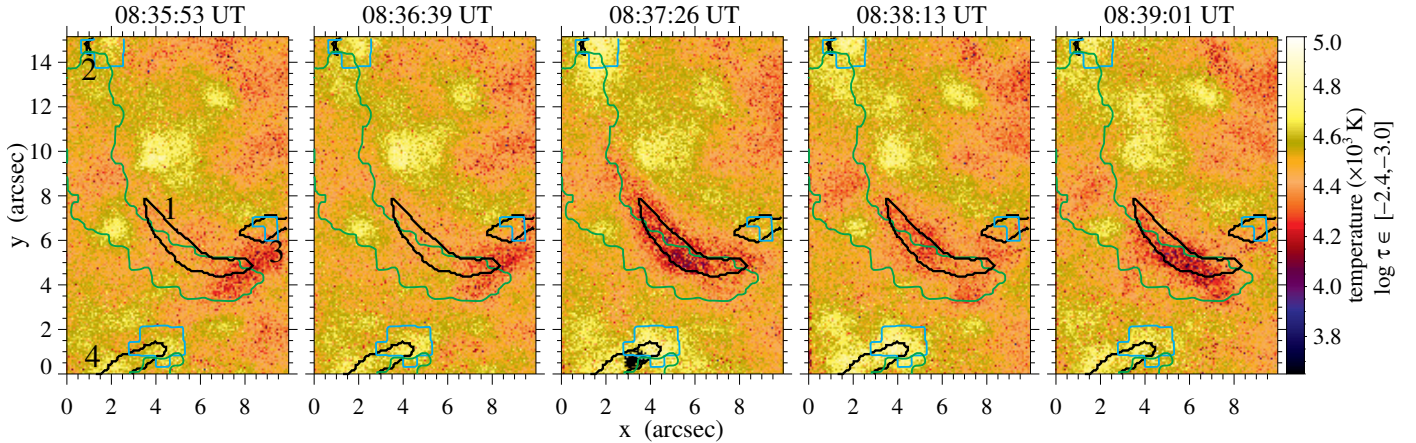


Fig. 5. Average temperature scans 16–20 (left to right) inferred from the NICOLE inversions of the Ca II 8542 Å line between the heights of $\log \tau \in [-2.4, -3.0]$. The time corresponds to the midpoint of each scan sequence. The impulsive phase starts at 08:37 UT. Overplotted black contours, marked with numbers 2–3 in the left-hand panel, show cumulative GFPI Ca II line-core enhancements between 08:37–08:39 UT. The black contour marked with 1 encompasses a dark filamentary structure seen in the GFPI Ca II line-core images. AIA 131 Å (green) and AIA 1600 Å (blue) contours show brightenings at 08:37:56 and 08:37:28 UT, respectively. The black area at the bottom of the panel at 08:37:26 UT does not show information on the inversions owing to bad fits (χ^2 exceeds threshold criterion). The FOV corresponds to the black rectangles shown in the GFPI panels of Fig. 2.

of Fig. 4. A few minutes later, at 08:30 UT, a negative-polarity patch gradually grows next to the right-hand solid red contour (area 3). The panel at 08:37 UT is highlighted by three red stars next to the contours indicating where the impulsive event started according to the Ca II spectra. The three brightening areas in the AIA 1600 Å channel are outlined with blue contours. They match the Ca II areas well. Immediately after this brightening, the most prominent flaring arch appeared in the hotter AIA channels, which was outlined by the orange contour in the AIA 131 Å filtergram. Another flaring arch (not shown) connected the upper and lower left-hand red stars. This is more distinct in images of AIA 94 Å (see Fig. 2), but also in all AIA wavelength bands except AIA 1600 and 1700 Å. Furthermore, the 08:37 UT panel is overlaid with three dotted contours: the black contour outlines the pore and the red contours the forming penumbra. Interestingly, next to the forming penumbra, a patch of negative polarity invaded the extensive positive polarity (see black arrow in Fig. 4). This intrusion became visible at 08:30 UT, was most prominent at 08:37 UT, lasted until 08:39 UT, and then slowly faded away. Although the negative polarity almost disappeared, the positive polarity did not fill the gap. However, a direct relation of this intrusion or the forming penumbra to the appearance of the brightenings cannot be established. Nevertheless, it indicates that the photospheric magnetic field was undergoing changes during this phase.

After overplotting the three areas of Ca II line-core enhancements (areas 2–4) onto the magnetograms, it becomes evident that each one shows different magnetic properties. One is rooted in the positive polarity (area 4), the other in the negative polarity (area 2), and the third touches mixed polarities, although mainly positive (area 3). The double arches seen in all high-energy AIA channels connected the negative polarity (area 2) with the positive (area 4) and mixed (area 3) polarities.

4.4. Temperature

We derived temperatures at different heights from the inversions of the Ca II 8542 Å spectra. We concentrated on a small region

(black rectangle in the GFPI panels of Fig. 2) that included the areas of interest (1–4) in the last five scans of the GFPI. In this way, we covered the pre-impulsive and impulsive phases. Atmospheric fluctuations on scales shorter than the photons mean-free path are irrelevant for the radiative transfer. Since we are not interested in such small-scale spurious fluctuations, the atmospheric parameters were averaged over a range of $\log \tau = 0.7$. In particular, Fig. 5 shows temperatures averaged over a range of $\log \tau \in [-2.4, -3.0]$, which corresponds to the upper photosphere. All panels are scaled between 3650 and 5000 K. The most relevant events were overplotted as contours: the Ca II line-core emission in areas 2–4 between 08:37–08:39 UT (black), the AIA 1600 Å brightening at 08:37 UT (blue), and the flaring arch seen in AIA 131 Å at 08:37 UT (green). Since area 1 had no line-core emission profiles, we set up a different criterion. We chose the most blueshifted profiles of the Ca II line by using filtergrams at $\Delta\lambda = -0.32$ Å from line center at 08:37 UT. For the contour, we selected profiles with the lowest intensity, that is, the deepest line core. Although the flaring arch contour from AIA 131 Å largely covers area 1, there is a small offset with respect to relevant temperature (and as seen later in the case of LOS velocity) changes.

The first two panels of Fig. 5 show the temperatures before the impulsive phase. The middle panel (08:37 UT) represents the beginning of the impulsive event. As expected, the temperature increases in areas 2–4. Conversely, the temperature in area 1 decreases. In the last panel, the temperature decreases gradually in areas 2–4, although the temperature decrease is fastest in area 3. The central area 1 remains cooler than in the pre-impulsive phase. Interestingly, area 1 shows an opposite behavior to the coronal channels of AIA, where brightenings appear in the same location (green contour), indicating increasing temperatures.

From a quantitative point of view, we summarized the temperature variations of the four areas in Table 1. First, we concentrate on the second half of the columns, which belong to average temperatures between $\log \tau \in [-2.4, -3.0]$ (shown in Fig. 5). The table exhibits the average and standard deviation of the temperature and the amount of pixels inside of each area. Scans 16 and 17 were acquired before the impulsive event. The impulsive event starts with scan 18 and shows an increase of 70–103 K

Table 1. Evolution of average temperature $\langle T \rangle$ and standard deviation σ_T inside of areas 1–4 that are marked in Fig. 5.

	Area	$\log \tau \in [-4.6, -5.2]$ (z_2)					$\log \tau \in [-2.4, -3.0]$ (z_1)				
		Scan					Scan				
		16	17	18	19	20	16	17	18	19	20
$\langle T \rangle$ (K)	1	5156	5199	5278	5194	5297	4408	4418	4283	4353	4313
σ_T (K)		801	811	837	899	1056	85	92	117	85	120
#		982	975	933	963	958	982	975	933	963	958
$\langle T \rangle$	2	5627	5383	5777	5844	6436	4566	4593	4669	4619	4632
σ_T		1195	973	1445	1546	1572	69	56	55	79	73
#		63	59	63	59	63	63	59	63	59	63
$\langle T \rangle$	3	5569	5598	6218	6183	6447	4463	4453	4533	4460	4472
σ_T		1220	1550	1611	1717	1654	88	101	86	94	77
#		341	336	331	320	336	341	336	331	320	336
$\langle T \rangle$	4	5590	5591	5900	6402	6498	4604	4627	4705	4714	4658
σ_T		1408	1695	1694	1773	1918	87	86	104	103	98
#		434	426	329	402	415	434	426	329	402	415

Notes. The row with the hashtag shows the number of pixels inside of each area. Note that the number varies because failed inversions were excluded (see threshold criterion in Sect. 3.3). The left and right blocks correspond to two different heights (z_1 and z_2), $\log \tau \in [-4.6, -5.2]$ and $\log \tau \in [-2.4, -3.0]$, respectively.

in areas 2–4 with respect to scan 16. Area 4 seems to be even hotter in scan 19. Nevertheless, we cannot rule out that scan 18 might have a higher temperature, but after ignoring pixels owing to bad fitting, the computed average temperature is lower. Area 1 behaves in a different way. At the beginning of the impulsive phase, the average temperature drops by 125 K with respect to scan 16. In the last two scans, the temperature increases and then decreases again, respectively.

We move farther up in the atmosphere and concentrate on a chromospheric height that shows a high sensitivity to temperature perturbations in the Ca II 8542 Å line. This is shown in the first half of the columns of Table 1, where we analyze the average temperature variations within $\log \tau \in [-4.6, -5.2]$. We first note that the standard deviation is one order of magnitude larger than in the $\log \tau \in [-2.4, -3.0]$ layer. In addition, the temperature itself is higher. In areas 2–4, the temperature increases by about 800–900 K between scans 16 and 20. Furthermore, in contrast to what we reported for the temperature between $\log \tau \in [-2.4, -3.0]$, the temperature continues to rise after the impulsive phase, that is, after scan 18. The highest temperatures occur in the last scan. Interestingly, at this height, area 1 shows a rise in temperature by about 140 K between the first and last scans. Although this increase is much weaker than the increase reported for areas 2–4, it is consistent with the increasing temperature seen in the higher AIA channels (see Fig. 2).

4.5. Line-of-sight velocity

Figure 6 compares the LOS velocities inferred from the Ca II 8542 Å line at three different atmospheric heights and along the five last GFPI scans. From top to bottom we are mapping from higher to lower layers of the atmosphere: line core (see Sect. 3.4), $\log \tau \in [-4.9, -5.5]$, and $\log \tau \in [-2.7, -3.3]$. The latter two are height ranges that are most sensitive to velocity variations according to the analyzed response functions (see Sect. 3.3.1). The FOV and the contours are the same as shown for the temperature in Fig. 3. The LOS velocities are scaled

between $\pm 4 \text{ km s}^{-1}$. Negative (positive) values denote blueshifts (redshifts) of the Ca II line.

The top panels plot the velocities retrieved from the Lorentzian fits of the line core. They serve as a first approximation since they often fail when more complex profiles appear. This is the case in the black areas in Fig. 6, which are mainly dominated by Ca II line-core emission profiles. In these regions, an inversion code such as NICOLE copes well with the more complex profiles, with the exception of few pixels in area 4 of the middle panel. After inspection, the line-core velocities represent a combination of the respective velocity maps shown in the middle and bottom rows. The velocities belonging to $\log \tau \in [-2.7, -3.3]$ (bottom row) show predominant blueshifts in the middle and lower half of the FOV. Conversely, the $\log \tau \in [-4.9, -5.5]$ velocities (middle row) show an enhancement of the blueshifts in the upper half of the FOV. Hence, the two heights extracted from the NICOLE inversions complement each other.

Figure 6 gives indications about the dynamics within the region of interest. The contours of area 1 (by definition represented by blueshifted Ca II profiles) and the flaring arch (green contour) show blueshifts during the five scans. In particular, the strongest blueshifts coincide with the middle scan at 08:37. This is consistent with the impulsive phase and the flaring arch seen in the AIA wavelength bands. Moreover, a large part of the Ca II blueshifts match the flaring arch. In contrast, areas 2–4 appear mainly redshifted. To support this qualitative finding, we present the average LOS velocities in Table 2. The table follows the same layout as Table 1. We first concentrate on the lowest height, which corresponds to $\log \tau \in [-2.7, -3.3]$. Area 1 consistently shows blueshifts of around -1.3 km s^{-1} before and after the impulsive event at 08:37 UT. The average velocity increases to -2.18 km s^{-1} during the impulsive phase. The remaining areas 2–4, which are distributed around area 1, exhibit redshifts before and after the impulsive phase. During the eruption, the velocities become negative, thus representing blueshifts. However, these blueshifts between -0.22 and -0.75 km s^{-1} are considerably lower than those seen in area 1.

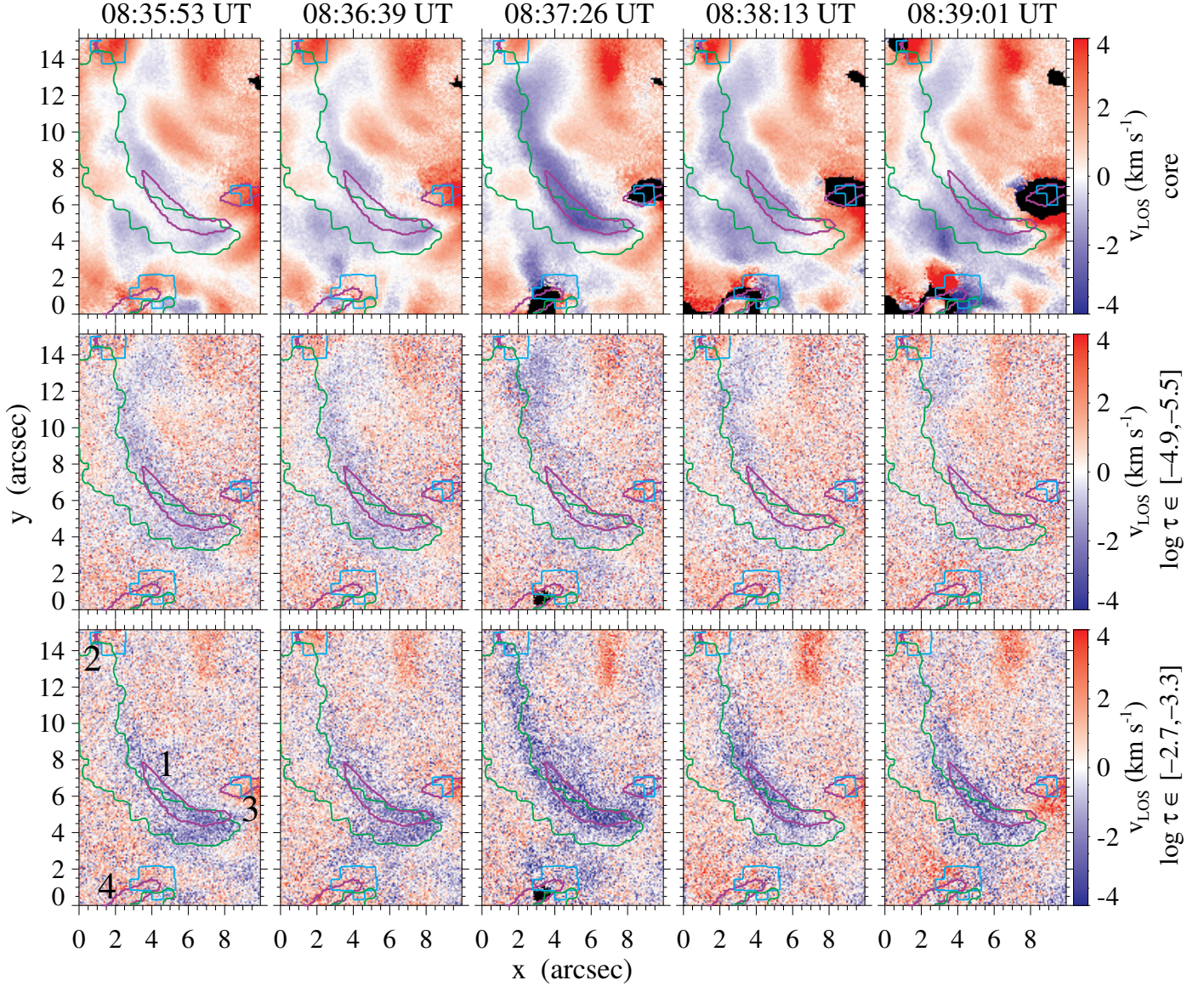


Fig. 6. *Top row:* LOS velocities retrieved from line-core Lorentzian fits. *Middle and bottom rows:* averaged velocities inferred with NICOLE between $\log \tau \in [-4.9, -5.5]$ and $\log \tau \in [-2.7, -3.3]$, respectively. The contours are the same as in Fig. 5, but switching black by purple. The impulsive phase starts at 08:37 UT.

Higher up in the chromosphere, between $\log \tau \in [-4.9, -5.5]$ (first half of the columns in Table 2), the plasma behaves differently. The retrieved velocities in area 1 still show blueshifts, but with a gradual decrease between scans 16 and 20, from -0.73 to -0.08 km s^{-1} , respectively. Furthermore, in the post-impulsive maps (after 08:37 UT), this drop in velocity is most noticeable. This is also evident in the velocity maps in the middle row in Fig. 2. Areas 2–4 are completely dominated by redshifts. In particular, area 3 exhibits an increased downflow (redshift) during the impulsive phase (an increase of about 0.70 km s^{-1} between scans 16 and 18). Area 4 manifests the most stable velocities, which fluctuate around 0.73 km s^{-1} .

An interesting observational feature occurs in the upper right part of the FOV in the $\log \tau \in [-2.7, -3.3]$ and line-core panels of Fig. 6. An elongated vertical patch of redshifts is present at position ($7''$, $14''$). A careful comparison with the GFPI panels in Fig. 2 yields that this patch does not coincide with the filamentary structure present in the FOV. The forming penumbra

from the large pore starts where the red patch ends. Therefore we speculate that flows might be interacting between these two structures. However, we do not find any direct relation to our impulsive event.

5. Discussion

5.1. Classification of the brightenings

We presented a multiwavelength analysis motivated by sudden small brightenings detected in Ca II 8542 Å line-core images. We identified three pronounced brightening areas (tagged with numbers 2–4 in all figures). The brightenings belonged to a large active region and had extensions up to $2'' \times 2''$. Next to the brightenings was a large pore with a slowly forming penumbra. Two of the brightenings were rooted in two different polarities (areas 2 and 4), while the third (area 3) resided next to mixed polarities, although the positive polarity dominated, in the photosphere.

Table 2. Same as Table 1, but for the average LOS velocities at $\log \tau \in [-4.9, -5.5]$ and $\log \tau \in [-2.7, -3.3]$.

	Area	$\log \tau \in [-4.9, -5.5]$ (z_2)					$\log \tau \in [-2.7, -3.3]$ (z_1)				
		16	17	Scan 18	19	20	16	17	Scan 18	19	20
$\langle v_{\text{LOS}} \rangle$ (km s ⁻¹)	1	-0.73	-0.61	-0.45	-0.07	-0.08	-1.22	-1.32	-2.18	-1.31	-1.28
σ_v (km s ⁻¹)		1.13	1.26	1.42	1.44	1.43	1.15	1.30	1.72	1.49	1.63
#		982	975	933	963	958	982	975	933	963	958
$\langle v_{\text{LOS}} \rangle$	2	0.38	0.25	0.38	0.18	0.64	0.73	0.72	-0.22	0.97	0.32
σ_v		1.46	1.46	1.27	1.39	1.45	1.46	1.25	1.18	1.05	1.68
#		63	59	63	59	63	63	59	63	59	63
$\langle v_{\text{LOS}} \rangle$	3	0.04	0.35	0.75	0.23	0.25	1.08	0.91	-0.75	0.99	1.12
σ_v		1.81	1.83	1.76	1.87	1.69	1.34	1.69	1.92	1.56	1.72
#		341	336	331	320	336	341	336	331	320	336
$\langle v_{\text{LOS}} \rangle$	4	0.72	0.67	0.68	0.75	0.79	0.28	0.73	-0.29	0.33	0.29
σ_v		1.65	1.66	1.65	1.56	1.69	1.71	1.83	2.43	2.03	2.23
#		434	426	329	402	415	434	426	329	402	415

Seen in Ca II spectra, line-core emission first started in areas 3 and 4, indicated by a clear reversal of the line-core intensity (Fig. 3). Area 2 also showed an enhanced line center that completely reversed in the last scan, about 1.5 min after the reversal in areas 3 and 4. The line-core emission remained until the end of the observations. The exact duration of the brightening was unknown, however, but a lower limit of 1.5 min can be established. At the same time, very close to these brightenings, three areas of about the same size flared up simultaneously in the AIA 1600 Å channel (arrows in Fig. 2 in the respective panel). All other AIA channels showed only one single but very intense brightening patch in area 4 (faint patch for AIA 1700 Å), which belonged to a high concentration of positive polarity. A few seconds later, hot arch-shaped structures appeared simultaneously in all chromospheric and coronal AIA channels, producing sufficiently high temperatures to ionize and recombine He II and Fe atoms (see online movie). Spontaneous smaller post-flaring events were also detected a few minutes later. The fact that the earlier brightenings in the AIA 1600 Å images lasted less than 24 s (time interval between AIA 1600 Å filtergrams) suggests that the brightenings belonged to the beginning of a microflare. We exclude EBs, IBs, and FAFs, since these events have substantially longer lifetimes in that wavelength band, even though Ca II 8542 Å line-core images show longer brightenings in time, at least 1.5 min, until the end of our observations.

The observed microflare shares an interesting feature with FAFs. Similar to the FAFs presented by [Vissers et al. \(2015\)](#), our observations showed very bright flaring arches next to the brightenings that lasted between 3.0–3.5 min (4 min in their case). The arch lengths were also similar ($\sim 20''$). Nevertheless, this might depend on the active region and the specific configuration of the magnetic field. Another unclear aspect is whether FAFs present spectral profiles with line-core emission. In [Vissers et al. \(2015\)](#), FAFs seem to have an enhanced intensity profile in H α , including the line core. The Ca II 8542 Å profiles shown in Fig. 3 clearly present line-core emission together with enhancements of the wings. The former fact makes them easily distinguishable from EBs, which only show strongly enhanced intensity line wings, but the core remains unaffected. We exclude IBs because they do not show brightenings in coronal wavelengths ([Peter et al. 2014](#)). This is another reason why we rule out EBs.

Further information on the nature of the studied brightenings might be provided by data from the Geostationary Operational Environmental Satellite system (GOES) or the Reuven Ramaty High Energy Solar Spectroscopic Imager (RHESSI; [Lin et al. 2002](#)). No increase in count rate was found in the GOES X-ray flux during our time range. However, the 6–12 keV band of RHESSI shows a sharp peak at exactly 08:37 UT, cotemporal to the beginning of the impulsive phase in our data. The 6–12 keV band is often used for flare detection algorithms ([Christe et al. 2008](#)) and is dominated by thermal emission ([Benz & Grigis 2002](#)). Thus, this provides another argument favoring the presence of an MF in our data.

5.2. Origin of the microflare

Following our argumentation, we consider our brightenings as part of an MF. We combine the available information to characterize the beginning of this MF. For the sake of clarity, we define two different layers (z_1 and z_2) to facilitate the interpretation of the height-dependent Ca II 8542 Å inversions. The velocities v_{z_1} and v_{z_2} refer to the mean LOS velocities in the intervals $\log \tau \in [-2.7, -3.3]$ and $\log \tau \in [-4.9, -5.5]$, respectively. Similarly, the temperatures T_{z_1} and T_{z_2} are defined as the averages in the intervals $\log \tau \in [-2.4, -3.0]$ and $\log \tau \in [-4.6, -5.2]$, respectively. The optical depth decreases with height. Therefore we identify z_1 with the upper photosphere and z_2 with the chromosphere.

5.2.1. Footpoints

The MF starts with one brightening that appeared simultaneously in the lowest and highest atmospheric layers of AIA, in area 4 in Fig. 2. This already distinguishes the analyzed MF from others that only exhibit emission in chromospheric layers and later present emission in the corona ([Brosius & Holman 2009](#)). At the same time, the Ca II 8542 Å line-core images from GFPI show brightenings in areas 3 and 4, and roughly 1.5 min later in area 2. Interestingly, one particular AIA 1600 Å filtergram shows the three brightenings at the beginning of the impulsive phase at 08:37 UT. This is clearly seen in Fig. 4 in the 08:37 UT panel. In this figure, the red contours represent the

Ca II line-core brightenings of areas 2–4, while the blue contours outline the AIA 1600 Å intensity enhancements. The two contours match fairly well (without taking into account projection effects). Therefore we consider areas 2–4 as the footpoints of the MF in the upper photosphere. They are rooted in opposite polarities. We conjecture that the mixed polarity patch at area 3, which emerged a few minutes before the beginning of the impulsive phase (Fig. 4), might have triggered magnetic field reconnection. Our observations favor a scenario with reconnection, which leads to sudden energy release. Whether this reconnection occurs in the photosphere or in higher layers of the atmosphere remains unclear from the available HMI magnetograms. Different polarities belong to the three brightenings, but the magnetograms before and after the beginning of the MF do not show a clear pattern of magnetic reconnection in the photosphere.

We now discuss the average LOS velocity changes associated with the footpoints inferred from the Ca II 8542 Å inversions. Before the impulsive phase, downflows dominate in all three areas at both heights (Fig. 6). These downflows are small, typically below 1.1 km s^{-1} (Table 2). We see a fundamental change in the upper photosphere at z_1 when the MF starts. All velocities in the three areas change their sign, switching from redshifts to blueshifts. The strongest upflows of $v_{z_1} = -0.75 \text{ km s}^{-1}$ are seen in area 3. This is the only area embedded in opposite magnetic polarities in the magnetograms. Conversely, higher in the atmosphere at z_2 , the downflows persist. This is consistent with bidirectional flows like those reported by Hong et al. (2016). However, their MF showed much higher LOS velocities, between $\pm 50 \text{ km s}^{-1}$, inferred also from the near-infrared Ca II line. The reason is probably that their MF was of GOES B-class, much more energetic than the MF studied in this work. The downflows at z_2 continue in the last two scans. After the impulsive phase, v_{z_1} returns to redshifts in all areas. We conclude that at the footpoints the impulsive phase of the MF produces sudden upflows of plasma from z_1 into higher atmospheric layers. However, these upflows are not seen above at z_2 . The origin of the bidirectional flows is unclear. A possible explanation is plasma evaporation and condensation. Nevertheless, inflows and outflows as a result of magnetic reconnection cannot be ruled out.

The temperature variations in the footpoints behave differently. All three areas show increases in their average temperature at both heights during the impulsive phase of the MF. Still, the temperature rise is much more noticeable at z_2 , that is, up to $\sim 600 \text{ K}$ compared to $\sim 80 \text{ K}$ at z_1 . Area 3 showed the largest increment at both heights. Interestingly, T_{z_2} continues to rise after the impulsive phase in all three areas, while T_{z_1} slowly decreases (Table 1). The larger and steeper temperature gradients in T_{z_2} compared to T_{z_1} argues in favor of placing the origin of the MF in higher layers. There is no clear evidence from the Ca II 8542 Å intensity spectra that the MF originates in the chromosphere. However, the consequences, such as temperature increments, are well detected there.

5.2.2. Flaring arches

The double arch-shaped brightenings seen in the AIA channels connect area 2 in the upper part of the FOV with areas 3 and 4 (Fig. 2). Hence, the flaring arches connect the three footpoints. The Ca II 8542 Å line-core images show a dark filamentary structure (area 1) fairly cospatially with the flaring arches (without taking projection effects into account). This filamentary structure is dominated by slow upflows at z_1 and z_2 (see area 1 in Table 2).

During the MF, the upflow becomes stronger, from $v_{z_1} = -1.32$ to -2.18 km s^{-1} . This is not evident at z_2 . The MF produces a lift-off of the plasma with moderate velocities at z_1 , that is, in the upper photosphere. However, the filamentary structure does not disappear, it remains visible in the Ca II 8542 Å line-core images after the MF. We speculate that uplifted plasma from area 1 during the impulsive phase might drain down along the flaring arches toward the footpoints after the MF. This explains the increased downflows in some footpoints at both heights after the MF (Table 2).

While the plasma in area 1 moves up during the MF, the average temperature T_{z_1} decreases by about 130 K. In contrast, T_{z_2} increases $\sim 80 \text{ K}$. An increment in T_{z_2} is consistent with the temperature enhancements detected in the hotter AIA channels.

Unfortunately, we are missing some part of the larger picture. This becomes clear as the cadences of AIA (12 s and 24 s) and the magnetograms of HMI (45 s) are not fast enough to reproduce the rapid evolution of the phenomena analyzed in this work. In addition, the long cadence of 47 s for the Ca II 8542 Å observations needs to be shortened in the future to capture rapid solar events. Higher time resolution is a great challenge that needs to be addressed by the new generation of solar telescopes, such as the Daniel K. Inouye Solar Telescope (DKIST; Tritschler et al. 2016) and the European Solar Telescope (EST; Matthews et al. 2016).

5.3. Line-of-sight velocity measurements

Two different techniques were used to determine the LOS velocities from the Ca II 8542 Å line. On the one hand, we used Lorentzian fits with four coefficients to approximate the spectral profile. This method ensured a fast computation of the line-core velocities. However, the fits failed when complex Ca II 8542 Å profiles were present (see black areas in Fig. 6). Moreover, there is no height-dependent information. On the other hand, the spectral-line inversion code NICOLE was used. It provided LOS velocities (and temperatures) at different heights in the atmosphere. Today, its main drawback is the computational power and time needed to invert the large number of profiles. Fortunately, the code has been parallelized recently, which makes the calculations substantially faster when high-performance computer clusters are available.

A comparison between both methods is shown in Fig. 6. Line-core fits to Ca II 8542 Å are not sufficient to study the physical quantities of fast-evolving events on the Sun. They are useful as quick-look information, but often miss the details encoded in complex spectral profiles. This is seen when comparing the two methods. The inversions reveal different velocities depending on the height. Especially at the footpoints, the velocities at z_1 and z_2 behave differently (Table 2). The detection of bidirectional flows was extracted from the inversions and is not detectable in the Lorentzian fits. For the Ca II 8542 Å line, we therefore recommend using more complex codes, such as inversion codes, to interpret the LOS velocities in fast events.

6. Summary and conclusions

We carried out a multiwavelength analysis of small brightening events in the solar atmosphere based on high-resolution spectroscopic images of the GFPI at GREGOR in the Ca II 8542 Å line. We combined the ground-based observations with images from AIA and HMI. The brightenings (areas 2–4 in all figures) were observed during their formation process and had sizes of

up to $2'' \times 2''$. We excluded EBs as well as IBs as an explanation of these brightenings. Several reasons supported this rejection: (1) our brightenings are clearly seen with AIA across all layers of the atmosphere up to the corona, while EBs and IBs do not have coronal counterparts; (2) our three brightenings were very short lived in AIA 1600 Å filtergrams (<24 s), while EBs have lifetimes of at least several minutes; and (3) the Ca II 8542 Å data showed emission in the line core, whereas spectra of EBs only show largely enhanced line wings, but no line-core emission. The scenario of a microflare appropriately fits our observations, although similarities to the FAFs reported by [Vissers et al. \(2015\)](#) were found. Like in their investigation, bright flaring arches were detected next to our brightenings. Furthermore, the lifetimes of these flaring arches were about 3.0–3.5 min with a size of $\sim 20''$. Simultaneous RHESSI observations showed a sharp increase in count rate in the 6–12 keV band, which further confirmed our event as a MF.

The three brightenings 2–4 in the Ca II 8542 Å line-core images were considered as the footpoints of the MF, whereas area 1 belonged to the flaring arches seen in AIA.

Height-dependent inversions of the Ca II 8542 Å intensity spectra with NICOLE revealed LOS velocities and temperatures before and during the impulsive phase of the MF. We focused on two specific height ranges, the upper photosphere (z_1) and the chromosphere (z_2).

- The MF heated the three footpoints at both heights. However, the temperature gradients during the impulsive phase were much steeper at z_2 (~ 600 K) than in z_1 (~ 80 K). After the impulsive phase, the temperatures at z_2 continued to rise at the footpoints, whereas they decreased at z_1 .
- The LOS velocities at the footpoints at both heights were dominated by downflows. However, during the impulsive phase, the velocities turned into blueshifts (up to -0.75 km s $^{-1}$) in the upper photosphere at z_1 . At z_2 , the velocities remained redshifted during the MF. This indicates bidirectional flows along the LOS.
- As a consequence of the MF, flaring double arches appeared in all AIA channels between the footpoints, except in 1600 and 1700 Å filtergrams. One of the flaring arches spatially coincided with a dark filamentary structure seen in the Ca II line-core image (area 1 in Fig. 2). From the inversions, we find that the plasma in the filamentary structure was predominantly moving upward before the MF occurred. During the impulsive phase, the plasma increased the upward motion at z_1 , reaching average LOS velocities of -2.18 km s $^{-1}$. After the impulsive phase, the plasma motion returned to the initial values for z_1 , and at z_2 the velocities dropped almost to zero. This scenario is consistent with rising plasma between the footpoints (along the filamentary structure seen in the Ca II line-core images), during the impulsive phase. At the same time, plasma is draining downward along the footpoints.
- The average temperatures in area 1 slightly increased (~ 80 K) at z_2 during the impulsive phase, which is consistent, but less than expected, with the hotter AIA channels, which became brighter. Conversely, the plasma became colder in the upper photosphere at z_1 at the same time.

We cannot answer the question where the microflare started. For a rapid solar event like an MF, we would need a better temporal and spectral resolution to distinguish the time and height of the start of the MF. The Ca II 8542 Å diagnostics suggest an origin above the Ca II line formation. The consequences of the MF are clearly reflected in the Ca II 8542 Å line, but they are less

dramatic than might be expected if magnetic reconnection occurred at this height. Spectropolarimetric observations to infer the vector magnetic field in higher layers of the solar atmosphere become crucial to answer this question.

Acknowledgements. The 1.5-m GREGOR solar telescope was built by a German consortium under the leadership of the Kiepenheuer-Institut für Sonnenphysik in Freiburg (KIS), with the Leibniz-Institut für Astrophysik Potsdam (AIP), the Institut für Astrophysik Göttingen (IAG), the Max-Planck-Institut für Sonnensystemforschung in Göttingen (MPS), and the Instituto de Astrofísica de Canarias (IAC), and with contributions by the Astronomical Institute of the Academy of Sciences of the Czech Republic (ASCR). The authors thank R.-E. Louis for his help during the observations. Rob Rutten, Gregal J.-M. Vissers, A. Warmuth, and H. Wang are greatly acknowledged for fruitful discussions. S.J.G.M. is grateful for financial support from the Leibniz Graduate School for Quantitative Spectroscopy in Astrophysics, a joint project of AIP and the Institute of Physics and Astronomy of the University of Potsdam, and he acknowledges support of the project VEGA 2/0004/16. Support from SOLARNET, a project supported by the European Commission's 7th Framework Program under grant agreement No. 312495, is greatly acknowledged. Finally, we are grateful for helpful comments of the anonymous referee that improved the quality of this publication.

References

- Bello González, N., Danilovic, S., & Kneer, F. 2013, *A&A*, **557**, A102
- Bentley, R. D., & Freeland, S. L. 1998, in *Crossroads for European Solar and Heliospheric Physics. Recent Achievements and Future Mission Possibilities*, ESA SP, 417, 225
- Benz, A. O., & Grigis, P. C. 2002, *Sol. Phys.*, **210**, 431
- Berkebile-Stoiser, S., Gömöry, P., Veronig, A. M., Rybák, J., & Sütterlin, P. 2009, *A&A*, **505**, 811
- Berlicki, A., & Heinzel, P. 2014, *A&A*, **567**, A110
- Berlicki, A., Heinzel, P., & Avrett, E. H. 2010, *Mem. Soc. Astron. It.*, **81**, 646
- Brosius, J. W., & Holman, G. D. 2009, *ApJ*, **692**, 492
- Canfield, R. C., & Metcalf, T. R. 1987, *ApJ*, **321**, 586
- Christe, S., Hannah, I. G., Krucker, S., McTiernan, J., & Lin, R. P. 2008, *ApJ*, **677**, 1385
- de la Cruz Rodríguez, J., Socas-Navarro, H., Carlsson, M., & Leenaarts, J. 2012, *A&A*, **543**, A34
- de la Cruz Rodríguez, J., Rouppe van der Voort, L., Socas-Navarro, H., & van Noort, M. 2013, *A&A*, **556**, A115
- De Pontieu, B., Title, A. M., Lemen, J. R., et al. 2014, *Sol. Phys.*, **289**, 2733
- DeRosa, M., & Slater, G. 2013, *Guide to SDO DATA Analysis*, Lockheed Martin Solar & Astrophysics Laboratory, Palo Alto, CA
- Ellerman, F. 1917, *ApJ*, **46**, 298
- Fang, C., Tang, Y.-H., & Xu, Z. 2006a, *Chin. Astron. Astrophys.*, **6**, 597
- Fang, C., Tang, Y. H., Xu, Z., Ding, M. D., & Chen, P. F. 2006b, *ApJ*, **643**, 1325
- Freeland, S. L., & Handy, B. N. 1998, *Sol. Phys.*, **182**, 497
- Georgoulis, M. K., Rust, D. M., Bernasconi, P. N., & Schmieder, B. 2002, *ApJ*, **575**, 506
- Gingerich, O., Noyes, R. W., Kalkofen, W., & Cuny, Y. 1971, *Sol. Phys.*, **18**, 347
- González Manrique, S. J., Kuckein, C., Pastor Yabar, A., et al. 2016, *Astron. Nachr.*, **337**, 1057
- Hannah, I. G., Christe, S., Krucker, S., et al. 2008, *ApJ*, **677**, 704
- Hong, J., Ding, M. D., Li, Y., et al. 2016, *ApJ*, **820**, L17
- Judge, P. G. 2015, *ApJ*, **808**, 116
- Kramida, A., Ralchenko, Y., Reader, J., & NIST ASD Team 2015, *National Institute of Standards and Technology Atomic Spectra Database* (ver. 5.3), [Online]. Available: <http://physics.nist.gov/asd>
- Kuckein, C., Denker, C., Verma, M., et al. 2017, in *Fine Structure and Dynamics of the Solar Atmosphere*, eds. S. Vargas Domínguez, A. G. Kosovichev, P. Antolin, & L. Harra, IAU Symp., 327, 20
- Leenaarts, J., de la Cruz Rodríguez, J., Kochukhov, O., & Carlsson, M. 2014, *ApJ*, **784**, L17
- Lemen, J. R., Title, A. M., Akin, D. J., et al. 2012, *Sol. Phys.*, **275**, 17
- Li, Z., Fang, C., Guo, Y., et al. 2015, *RA&A*, **15**, 1513
- Lin, R. P., Schwartz, R. A., Kane, S. R., Pelling, R. M., & Hurley, K. C. 1984, *ApJ*, **283**, 421
- Lin, R. P., Dennis, B. R., Hurford, G. J., et al. 2002, *Sol. Phys.*, **210**, 3
- Liu, C., Qiu, J., Gary, D. E., Krucker, S., & Wang, H. 2004, *ApJ*, **604**, 442
- Löfdahl, M. G. 2002, in *Image Reconstruction from Incomplete Data*, eds. P. J. Bones, M. A. Fiddy, & R. P. Millane, Proc. SPIE, 4792, 146
- Matsumoto, T., Kitai, R., Shibata, K., et al. 2008, *PASJ*, **60**, 577
- Matthews, S. A., Collados, M., Mathioudakis, M., & Erdelyi, R. 2016, in *Ground-based and Airborne Instrumentation for Astronomy VI*, Proc. SPIE, 9908, 990809

- Neckel, H., & Labs, D. 1984, *Sol. Phys.*, **90**, 205
- Nelson, C. J., Doyle, J. G., Erdélyi, R., et al. 2013, *Sol. Phys.*, **283**, 307
- Pariat, E., Schmieder, B., Berlicki, A., et al. 2007, *A&A*, **473**, 279
- Pariat, E., Masson, S., & Aulanier, G. 2009, *ApJ*, **701**, 1911
- Pesnell, W. D., Thompson, B. J., & Chamberlin, P. C. 2012, *Sol. Phys.*, **275**, 3
- Peter, H., Tian, H., Curdt, W., et al. 2014, *Science*, **346**, 1255726
- Puschmann, K. G., Denker, C., Kneer, F., et al. 2012, *Astron. Nachr.*, **333**, 880
- Quintero Noda, C., Shimizu, T., de la Cruz Rodríguez, J., et al. 2016, *MNRAS*, **459**, 3363
- Reid, A., Mathioudakis, M., Doyle, J. G., et al. 2016, *ApJ*, **823**, 110
- Rezaei, R., & Beck, C. 2015, *A&A*, **582**, A104
- Rutten, R. J. 2016, *A&A*, **590**, A124
- Rutten, R. J., Vissers, G. J. M., Rouppe van der Voort, L. H. M., Sütterlin, P., & Vitas, N. 2013, *J. Phys. Conf. Ser.*, **440**, 012007
- Scherrer, P. H., Schou, J., Bush, R. I., et al. 2012, *Sol. Phys.*, **275**, 207
- Schmidt, W., von der Lühe, O., Volkmer, R., et al. 2012, *Astron. Nachr.*, **333**, 796
- Schmieder, B., Rust, D. M., Georgoulis, M. K., Démoulin, P., & Bernasconi, P. N. 2004, *ApJ*, **601**, 530
- Socas-Navarro, H., Martínez Pillet, V., Elmore, D., et al. 2006, *Sol. Phys.*, **235**, 75
- Socas-Navarro, H., de la Cruz Rodríguez, J., Asensio Ramos, A., Trujillo Bueno, J., & Ruiz Cobo, B. 2015, *A&A*, **577**, A7
- Tian, H., Xu, Z., He, J., & Madsen, C. 2016, *ApJ*, **824**, 96
- Tritschler, A., Rimmele, T. R., Berukoff, S., et al. 2016, *Astron. Nachr.*, **337**, 1064
- van Noort, M., Rouppe van der Voort, L., & Löfdahl, M. G. 2005, *Sol. Phys.*, **228**, 191
- Vissers, G. J. M., Rouppe van der Voort, L. H. M., & Rutten, R. J. 2013, *ApJ*, **774**, 32
- Vissers, G. J. M., Rouppe van der Voort, L. H. M., Rutten, R. J., Carlsson, M., & De Pontieu, B. 2015, *ApJ*, **812**, 11
- Volkmer, R., Eisenträger, P., Emde, P., et al. 2012, *Astron. Nachr.*, **333**, 816
- Wöger, F., & von der Lühe, O. 2008, in *Advanced Software and Control for Astronomy II*, Proc. SPIE, 7019, 70191